Journal of Computational Physics **159,** 13–37 (2000)
doi:10.1006/jcph.2000.6422, available online at http://www.idealibrary.com on IDEAL®

Numerical Modeling of Optical Gradient Traps Using the Vector Finite Element Method[1]

Daniel A. White

Center for Applied Scientific Computing, Lawrence Livermore National Laboratory, P.O. Box 808 M/S L-560, Livermore, California 94551
E-mail: dwhite@llnl.gov

Received March 2, 1999; revised October 12, 1999

It has been established that under certain conditions microscopic dielectric objects can be trapped by a tightly focused laser beam. This phenomenon is commonly referred to as an optical gradient trap. The recently developed vector finite element method is used to visualize the interaction of the laser beam with the dielectric object and to quantitatively predict the optical trapping efficiency. The vector finite element method is an accurate and efficient approach when the incident beam wavelength is comparable to the object size, and it has the advantage that it can be used to model the trapping of arbitrarily shaped 3D objects.

1. INTRODUCTION

It is well known that light waves have momentum and that this momentum can be transfered to a solid object. This is often referred to as radiation pressure. It was first demonstrated in 1970 that the force of radiation pressure could accelerate a micrometer-sized polystyrene sphere [1]. Later it was demonstrated that the sphere could be levitated by balancing the force of radiation pressure against the force of gravity [2]. In these experiments it was observed that the force was predominately in the direction of power flow, with a slight transverse force toward the center of the beam. In 1986 it was shown experimentally that a microscopic dielectric object could be trapped by a tightly focused laser beam [3]. This is referred to as a single-beam optical gradient trap, or "optical tweezers." The optical trapping force has been measured for dielectric spheres under a variety of conditions [4–6]. The trapping force depends on many factors including the size and dielectric constant of the object, the wavelength and polarization of the laser beam, and the position of the object with respect to the beam focus spot. The predominate application of optical traps is microbiology, where optical traps have been used for the manipulation of cells [7–9] and the manipulation

[1] This work was supported in part by the U.S. Department of Energy under Grant W-7405-Eng-48.

0021-9991/00 $35.00

of viruses and bacteria [10, 11]. As another biological application, a properly calibrated optical trap can be used to measure minute biological forces [12–14] within living cells.

Several different approaches for the theoretical modeling of optical gradient traps have been investigated. In the geometrical optics (GO) approach the incident laser beam is modeled by a collection of independent light rays [15–17]. These rays intersect the surface of the dielectric object and are refracted/reflected according to the classic Fresnel formula. In practice each ray is traced for only a few reflections. Each ray carries momentum, and this momentum changes direction as the ray is refracted and reflected. The net force on the dielectric object is then computed by summing the contribution of momentum transfer from each individual ray. Since the force is proportional to the incident power it is common to introduce the optical trapping efficiency

$$Q = \frac{cF}{nP}, \tag{1}$$

where F is a component of the force, P is the power, c is the speed of light, and n is the index of refraction. By convention the object is trapped if $Q > 0$. GO modeling predicts that dielectric objects will be trapped only for particular values of n. For example, GO modeling predicts that reflecting spheres and dielectric spheres with $n < 1$ will be pushed away from the beam focus spot, rather than being trapped, which is in agreement with experimental data. In addition GO modeling predicts that extreme beam cone angles are required for trapping to occur, which is also in agreement with experiment. However, the GO model is an asymptotic approximation and hence the predicted Q agrees with measured values only for large spheres. This is a significant disadvantage of the GO model, since for most applications the object size is comparable to the incident beam wavelength.

Several researchers have proposed modeling optical gradient traps using a finite series approximate solution of Maxwell's equations [4, 18, 19]. This approach yields accurate full-wave electromagnetic fields within, and on the surface of, the dielectric sphere. The primary difficulty with this approach is modeling the incident laser beam; however, fairly accurate approximations of Gaussian beams have been developed [20]. Given the approximate electromagnetic field on the surface of the sphere, the optical trapping force can be computed by integrating the dot product of the surface outward normal with the Maxwell stress tensor over the surface of the sphere. Optical trapping efficiencies computed in this manner correlate well with measured values. The disadvantage of this approach is that it is only valid for spheres or other simple shapes that admit to a series solution of Maxwell's equations.

In this paper, a vector finite element method is used to model an optical gradient trap. The method solves Maxwell's equations on an unstructured three-dimensional grid using edge vector finite elements as a basis for the electric field and face vector finite elements for the magnetic flux density. The method described in this paper is a generalization of that originally proposed in [21]. The convergence of the method has been theoretically analyzed by several researchers [22–25], and computational efficiency of the method has been investigated [26]. There are several advantages of the vector finite element compared to other grid-based methods such as nodal finite element, finite volume, and finite difference methods. First, the method accurately models the discontinuity of the electric field across material interfaces, which is particularly important for modeling optical gradient traps. Second, the method is provably stable and energy conserving even for highly distorted grids. Third, the method accurately models the divergence (or lack thereof) of fields and

fluxes. The accurate modeling of the divergence is related to the problem of spurious modes [27, 28], which often plague traditional nodal finite element methods. Since there are several different variants of the vector finite element method, the method used in this study will be derived below. The procedure for modeling an optical gradient trap is described in detail, and predicted trapping efficiencies for microspheres are compared to measured values. The computed trapping efficiencies compare well (withing the measured error bounds), confirming the utility of the vector finite element method for optical force calculations.

2. VECTOR FINITE ELEMENT METHOD

There are a variety of ways to express Maxwell's equations; in this paper the electric field $\vec{E}$ and the magnetic flux density $\vec{B}$ are used as the principle variables. Maxwell's equations for the electromagnetic fields in an inhomogeneous volume Ω are

$$\mu^{-1}\frac{\partial}{\partial t}\vec{B} = -\mu^{-1}\nabla\times\vec{E} - \mu^{-1}\sigma_M\mu^{-1}\vec{B} \tag{2}$$

$$\epsilon\frac{\partial}{\partial t}\vec{E} = \nabla\times\mu^{-1}\vec{B} - \sigma_E\vec{E} \tag{3}$$

$$\nabla\cdot\epsilon\vec{E} = 0 \tag{4}$$

$$\nabla\cdot\vec{B} = 0. \tag{5}$$

Note that we have assumed zero charge density. The dielectric permittivity ϵ, the magnetic permeability μ, and the conductivities σ_E and σ_M are assumed to be symmetric positive-definite tensors, which are functions of position only. The initial conditions and boundary conditions are given by

$$\vec{E}(t=0) = \vec{E}_{\text{ic}}, \quad \vec{B}(t=0) = \vec{B}_{\text{ic}} \qquad \text{in } \Omega \tag{6}$$

$$\vec{n}\times\vec{E} = \vec{E}_{\text{BC}} \qquad \text{on } \Gamma. \tag{7}$$

In addition, for the problem to be well-posed we require that the independent magnetic and electric current sources satisfy

$$\nabla\cdot\vec{M} = 0, \qquad \nabla\cdot\vec{J} = 0. \tag{8}$$

The variational form of the above PDE is as follows: find $\vec{E} \in H(\text{curl}, t)$ and $\vec{B} \in H(\text{div}, t)$ such that

$$\frac{\partial}{\partial t}(\epsilon\vec{E}, \vec{E}^*) = (\mu^{-1}\nabla\times\vec{E}^*, \vec{B}) - (\sigma_E\vec{E}, \vec{E}^*) - (\vec{J}, \vec{E}^*), \tag{9}$$

$$\frac{\partial}{\partial t}(\mu^{-1}\vec{B}, \vec{B}^*) = -(\mu^{-1}\nabla\times\vec{E}, \vec{B}^*) - (\mu^{-1}\sigma_M\mu^{-1}\vec{B}, \vec{B}^*) - (\mu^{-1}\vec{M}, \vec{B}^*), \tag{10}$$

for all $\vec{E}^* \in H_0(\text{curl}, t)$ and $\vec{B}^* \in H_0(\text{div}, t)$. The solution spaces are defined by

$$H(\text{curl}, t) = \{\vec{u(t)} : \vec{u(t)} \in (L(\Omega))^3; \nabla\times\vec{u(t)} \in (L(\Omega))^3\}, \tag{11}$$

$$\|\vec{u(t)}\|_{H(\text{curl})} = (\|\vec{u(t)}\|^2 + \|\nabla\times\vec{u(t)}\|^2)^{1/2}, \tag{12}$$

and

$$H(\mathrm{div}, t) = \{\vec{u(t)} : u, \vec{t} \in (L(\Omega))^3; \nabla \cdot \vec{u(t)} \in (L(\Omega))^3\}, \tag{13}$$

$$\|\vec{u(t)}\|_{H(\mathrm{div},t)} = (\|u, \vec{t}\|^2 + \|\nabla \cdot \vec{u(t)}\|^2)^{1/2}. \tag{14}$$

The test spaces are defined by

$$H_0(\mathrm{curl}, t) = \{\vec{u(t)} : \vec{u(t)} \in H(\mathrm{curl}); \hat{n} \times \vec{u(t)} = 0 \text{ on } \Gamma\}, \tag{15}$$

$$H_0(\mathrm{div}, t) = \{\vec{u(t)} : \vec{u(t)} \in H(\mathrm{div}); \hat{n} \cdot \vec{u(t)} = 0 \text{ on } \Gamma\}. \tag{16}$$

This variational form of Maxwell's equations is a generalization of that proposed in [21] to include conductivities. Equation (10) can be derived by multiplying (2) by the test function $\vec{B}^*$ and integrating over Ω. Likewise (9) can be derived by multiplying (3) by the test function $\vec{E}^*$, integrating over Ω, and employing the identity $\nabla \cdot (a \times b) = b \cdot (\nabla \times a) - a \cdot (\nabla \times b)$ and the divergence theorem. One interpretation of the above variational form is that the solution must satisfy Poynting's theorem of energy conservation for every test function $\vec{E}^*$ and $\vec{B}^*$.

The variational form (9)–(10) is discretized using the hexahedral vector finite elements defined in [21]. The electric field is approximated as a linear combination of edge elements.

$$\vec{E} = \sum_{i=1}^{N_e} \alpha_i(t) \vec{W}_i, \tag{17}$$

where N_e is the number of edges in the mesh. The electric field given by (17) is a first-order approximation to the true field when using the norm (12). The basis functions $\vec{W}$ are conforming with the space $H(\mathrm{curl})$. These functions are called edge functions because they have the property

$$\int \vec{W}_i \cdot \hat{t}_j = \delta_{ij}, \tag{18}$$

where $\hat{t}_j$ is the unit tangent along edge j. Hence the degrees-of-freedom α_i are given by

$$\alpha_i = \int \vec{E} \cdot \hat{t}_i \tag{19}$$

and can be interpreted as the voltage along edge i of the mesh. The magnetic flux density is approximated as a linear combination of face elements,

$$\vec{B} = \sum_{i=1}^{N_f} \beta_i(t) \vec{F}_i, \tag{20}$$

where N_f is the number of faces in the mesh. The magnetic flux density given by (20) is a first-order approximation to the true flux density when using the norm (14). The basis functions $\vec{B}$ are conforming with the space H (div). These functions are called face functions because they have the property

$$\int \vec{B}_i \cdot \hat{n}_j = \delta_{ij}, \tag{21}$$

where $\hat{n}_j$ is the unit normal to face j. Hence the degrees-of-freedom β_i are given by

$$\beta_i = \int \vec{B} \cdot \hat{n}_i \, da \tag{22}$$

and can be interpreted as the magnetic flux through face i of the mesh.

The edge and face finite elements satisfy the same inclusion relations as their associated Hilbert spaces. Let V denote the space of linear nodal elements, let W denote the space of linear edge elements, let F denote the space of linear face elements, and let S denote the space of piecewise-constant scalar functions. These spaces satisfy

$$\text{If } \Phi \in V \qquad \text{then } \nabla\Phi \in W, \tag{23}$$

$$\text{If } \vec{E} \in W \qquad \text{then } \nabla \times \vec{E} \in F, \tag{24}$$

$$\text{If } \vec{B} \in F \qquad \text{then } \nabla \cdot \vec{B} \in S. \tag{25}$$

These inclusion relations are used in Section 3 below to prove some important properties of the vector finite element method.

Using the approximations (17) and (20) in the variational form of Maxwell's equations yields a coupled system of ordinary differential equations

$$\mathbf{C}\frac{\partial}{\partial t}\alpha(t) = \mathbf{K}^T\beta(t) - \mathbf{G}\alpha(t) - \mathbf{R}j(t), \tag{26}$$

$$\mathbf{D}\frac{\partial}{\partial t}\beta(t) = -\mathbf{K}\alpha(t) - \mathbf{P}\beta(t) - \mathbf{D}m(t), \tag{27}$$

where the matrices are given by

$$\mathbf{C}_{ij} = (\epsilon\vec{W}_i, \vec{W}_j), \tag{28}$$

$$\mathbf{K}_{ij} = (\mu^{-1}\nabla \times \vec{W}_i, \vec{F}_j), \tag{29}$$

$$\mathbf{G}_{ij} = (\sigma_E\vec{W}_i, \vec{W}_j), \tag{30}$$

$$\mathbf{R}_{ij} = (\vec{W}_i, \vec{F}_j), \tag{31}$$

$$\mathbf{D}_{ij} = (\mu^{-1}\vec{F}_i, \vec{F}_j), \tag{32}$$

$$\mathbf{P}_{ij} = \left(\frac{\sigma_M}{\mu^2}\vec{F}_i, \vec{F}_j\right). \tag{33}$$

The above system of ODEs is integrated in time using the second-order central difference "leapfrog" method. In this method the electric degrees-of-freedom are known at whole time steps, and the magnetic degrees-of-freedom are known at the half time steps. Using superscript n to denote the time level, we integrate the ODE according to

$$\left(\mathbf{C} + \frac{\Delta t}{2}\mathbf{G}\right)\alpha^{n+1} = \Delta t\mathbf{K}^T\beta^{n+1/2} + \left(\mathbf{C} - \frac{\Delta t}{2}\mathbf{G}\right)\alpha^n - \mathbf{R}j^n, \tag{34}$$

$$\left(\mathbf{D} + \frac{\Delta t}{2}\mathbf{P}\right)\beta^{n+1/2} = -\Delta t\mathbf{K}\alpha^n + \left(\mathbf{D} - \frac{\Delta t}{2}\mathbf{P}\right)\beta^{n-1/2} - \Delta t\mathbf{D}m^{n+1/2}. \tag{35}$$

This integration requires the solution of large, sparse, linear systems at every time step. In this study the incomplete Cholesky preconditioned conjugate gradient (ICCG) is used; the

performance of this method for these particular linear systems is documented elsewhere [26, 29].

3. ANALYSIS

3.1. *Stability and Conservation of Energy*

Numerical stability is always an issue when solving PDEs on unstructured grids. Several proposed finite difference and finite volume methods have been shown to be unconditionally unstable for distorted hexahedral grids. In this section we show, using matrix stability analysis, that the vector finite element method described above is conditionally stable.

Consider a closed, source-free region with the boundary condition $\hat{n} \times \vec{E} = 0$ on the boundary. There is some initial electromagnetic field distribution and these fields are updated in time according to (34) and (35). For simplicity assume lossless media. The simplified update equations become

$$\mathbf{C}\alpha^{n+1} = \Delta t \mathbf{K}^T \beta^{n+1/2} + \mathbf{C}\alpha^n, \tag{36}$$

$$\mathbf{D}\beta^{n+1/2} = -\Delta t \mathbf{K}\alpha^n + \mathbf{D}\beta^{n-1/2}. \tag{37}$$

The matrices $\mathbf{C}$ and $\mathbf{D}$ are symmetric positive definite and hence have Cholesky decompositions $\mathbf{C} = \tilde{\mathbf{C}}^T\tilde{\mathbf{C}}$ and $\mathbf{D} = \tilde{\mathbf{D}}^T\tilde{\mathbf{D}}$, respectively. We define new degrees of freedom

$$\tilde{\alpha} = \tilde{\mathbf{C}}\alpha \tag{38}$$

$$\tilde{\beta} = \tilde{\mathbf{D}}\beta. \tag{39}$$

The leapfrog update can now be expressed in amplification matrix form as

$$\begin{bmatrix} \tilde{\alpha}^{n+1} \\ \tilde{\beta}^{n+1/2} \end{bmatrix} = \begin{bmatrix} (I - \Delta t^2 \mathbf{Q}\mathbf{Q}^T) & \Delta t \mathbf{Q} \\ -\Delta t \mathbf{Q}^T & I \end{bmatrix} \begin{bmatrix} \tilde{\alpha}^{n} \\ \tilde{\beta}^{n-1/2} \end{bmatrix}, \tag{40}$$

where the matrix Q is given by

$$\mathbf{Q} = \tilde{\mathbf{C}}^{-T}\mathbf{K}^T\tilde{\mathbf{D}}^{-1}. \tag{41}$$

It can be shown [26] that that the stability condition is

$$\Delta t \leq \frac{2}{\sqrt{\max(\xi)}}, \tag{42}$$

where ξ is the set of eigenvalues of the eigenproblem

$$\mathbf{Q}\mathbf{Q}^T z = \xi z. \tag{43}$$

When (42) is satisfied all the eigenvalues of the amplification matrix are unity. In general this is not sufficient to prove stability but in this case there exists a complete set of linearly independent eigenvectors and the method is neutrally stable. The denominator $\sqrt{\max(\xi)}$ has units of frequency and can be interpreted as the highest frequency that can be supported

by the grid, and the stability condition is simply that the electromagnetic fields must be sampled at (or above) the Nyquist rate.

It is straightforward to relate the above stability analysis to conservation of energy. The integral form of Poynting's theorem is

$$\oint_\Gamma \mu^{-1}\vec{E}\times\vec{B}\cdot\hat{n}\,d\Gamma+\int_\Omega \mu^{-1}\vec{B}\cdot\vec{M}\,d\Omega+\int_\Omega \vec{E}\cdot\vec{J}\,d\Omega+\int_\Omega \frac{\sigma_M}{\mu}\vec{B}\cdot\vec{B}\,d\Omega$$
$$+\int_\Omega \sigma_E\vec{E}\cdot\vec{E}\,d\Omega+\int_\Omega \frac{\sigma_1}{\mu}\vec{B}\cdot\frac{\partial}{\partial t}\vec{B}\,d\Omega+\int_\Omega \epsilon\vec{E}\cdot\frac{\partial}{\partial t}\vec{E}\,d\Omega=0. \tag{44}$$

The first term can be expanded as

$$\oint_\Gamma \mu^{-1}\vec{E}\times\vec{B}\cdot\hat{n}\,d\Gamma=\int_\Omega \mu^{-1}\vec{B}\cdot\nabla\times\vec{E}\,d\Omega-\int_\Omega \mu^{-1}\vec{E}\cdot\nabla\times\vec{B}\,d\Omega. \tag{45}$$

Now, using the degrees-of-freedom α and β and the matrices defined in (28)–(33), the discretized version of Poynting's theorem is

$$\beta^T\mathbf{K}\alpha-\alpha^T\mathbf{K}_T\beta+\beta^T\mathbf{D}m+\alpha^T\mathbf{R}_j+\beta^T\mathbf{P}\beta+\alpha^T\mathbf{G}\alpha+\beta^T\mathbf{D}\frac{\partial}{\partial t}\beta+\alpha^T\mathbf{C}\frac{\partial}{\partial t}\alpha=0. \tag{46}$$

The combined first two terms represent the net power flow into the domain. The term $\beta^T\mathbf{D}m$ and $\alpha^T\mathbf{R}j$ represent the power put into the domain by the independent magnetic and electric current sources, respectively. The terms $\beta^T\mathbf{P}\beta$ and $\alpha^T\mathbf{G}\alpha$ represent the power dissipated due to the magnetic and electric conductivities, respectively, The last two terms $\beta^T\mathbf{D}\frac{\partial}{\partial t}\beta$ and $\alpha^T\mathbf{C}\frac{\partial}{\partial t}\alpha$ represent the time rate of change of stored magnetic and electric energy. For the simplified situation of no net power flow into the domain, no independent current sources in the domain, and no lossy media in the domain, the time rate of change of the combined magnetic and electric energy must be zero. For any stable time step Δt we have

$$(\tilde{\alpha}^{n+1})^T\tilde{\alpha}^{n+1}+(\tilde{\beta}^{n+1/2})^T\tilde{\beta}^{n+1/2}=(\tilde{\alpha}^{n})^T\tilde{\alpha}^{n}+(\tilde{\beta}^{n-1/2})^T\tilde{\beta}^{n+1/2}, \tag{47}$$

which is equivalent to

$$(\alpha^{n+1})^T\mathbf{C}\alpha^{n+1}+(\beta^{n+1/2})^T\mathbf{D}\beta^{n+1/2}=(\alpha^{n})^T\mathbf{C}\alpha^{n}+(\beta^{n-1/2})^T\mathbf{D}\beta^{n-1/2}, \tag{48}$$

and the electromagnetic energy is indeed constant. This is important for electromagnetic problems that require long time integration intervals.

3.2. *Conservation of Magnetic Charge*

If the initial magentic flux density is divergence free (zero magnetic charge density everywhere) and the numerical method conserves magnetic charge, then the flux density will remain divergence free for all time. Magnetic charge will be conserved if

$$\nabla\cdot\frac{\partial}{\partial t}\vec{B}=0. \tag{49}$$

everywhere, or alternatively

$$\oint_\Gamma \frac{\partial}{\partial t}\vec{B}\cdot\hat{n}\,d\Gamma=0, \tag{50}$$

where the integral is over any particular hexahedral volume in the grid. In terms of the degrees-of-freedom this can be expressed as

$$\sum_{i=1}^{6} \frac{\partial}{\partial t}\beta_i = 0, \tag{51}$$

since the degrees-of-freedom β_i are precisely the net magnetic flux through face i. These degrees-of-freedom are computed via the magnetic field ODE (27).

Define the subspace

$$F_0 = \{\vec{u} \in F; \nabla \cdot \vec{u} = 0\}. \tag{52}$$

An important property of the vector finite element space W and F is that the operator $\nabla\times$ is surjective from W to F_0 [21]; the curl of every function in W can be written as a linear combination of functions in F_0. Therefore for any electric field, the magnetic flux density computed via (27) satisfies (51) exactly. This is analogous to charge conservation with finite volume methods that place the electric field on mesh edges and the magnetic field on mesh faces [30, 31].

3.3. *Conservation of Electric Charge*

The electric field is approximated as a linear combination of edge elements. Since these elements do not have normal continuity across cell faces, the electric field is not divergence free in the traditional sense. Rather the electric field is divergence free only in the variational sense. The variational form of (4) is

$$\int_\Omega \Phi(\nabla \cdot \epsilon\vec{E})\, d\Omega = -\int_\Omega \epsilon\vec{E} \cdot \nabla\Phi\, d\Omega + \oint_\Gamma \Phi\epsilon\vec{E} \cdot \hat{n}\, d\Gamma = 0, \tag{53}$$

where Φ is a continuous piecewise linear function. Since the field is not required to be divergence free on the boundary Γ we can choose $\Phi = 0$ on Γ and the last term in (53) is zero. Since it can be assumed that the initial electric field satifies (53), the requirement for electric charge conservation is

$$\left(\frac{\partial}{\partial t}\epsilon\vec{E}, \nabla\Phi\right) = 0, \tag{54}$$

for all $\Phi \in H$ (grad).

Define the subspace

$$W_0 = \{\vec{v} \in W; \nabla \times \vec{v} = 0\}. \tag{55}$$

An important property of the vector finite element spaces W and V is that the operator ∇ is surjective from V to W_0, the gradient of every function in V can be written as a linear combination of functions in W_0. Let ω be the vector of degrees of freedom of some vector function $\Omega \in W_0$. The null space of the matrix K in (27) is W_0, i.e., $K\omega = 0$ for all $\Omega \in W_0$. The discrete version of (54) is then

$$\omega^T \mathbf{C} \frac{\partial}{\partial t}\alpha(t) = 0 \tag{56}$$

for all $\Omega \in W_0$. That the above equation is satisfied can be seen by taking the dot product of an arbitray ω with the electric field ODE (26) (assuming zero conductivity and no current source), which yields

$$\omega^T \mathbf{C} \frac{\partial}{\partial t} \alpha(t) = \omega^T \mathbf{K}^T \beta(t) = \beta(t)^T \mathbf{K} \omega = 0 \tag{57}$$

for all $\Omega \in W_0$. Therefore a variational form of charge conservation is satisfied for all time. This is true independent of any distortions in the mesh, which is an important property of the vector finite element method.

4. MODELING THE OPTICAL GRADIENT TRAP

A three-dimensional hexahedral grid is used to model the dielectric object and the surrounding medium. The grid is in the shape of a large sphere, with the dielectric object near the center of the sphere. An example grid is shown in Fig. 1. The initial electromagnetic fields in the computational domain are zero. A time varying source is used to launch the laser beam into the computational domain. This source is designed such that the laser beam comes to a focus at the center of the grid. The frequency of the laser and the beam cone angle are user-specified parameters. Since the computational domain is finite, the cross section of the incicdent beam is also finite. Rather than abrubtly truncating a Gaussian or polynomial profile, which would introduce artificial high-frequency components, the beam is modeled

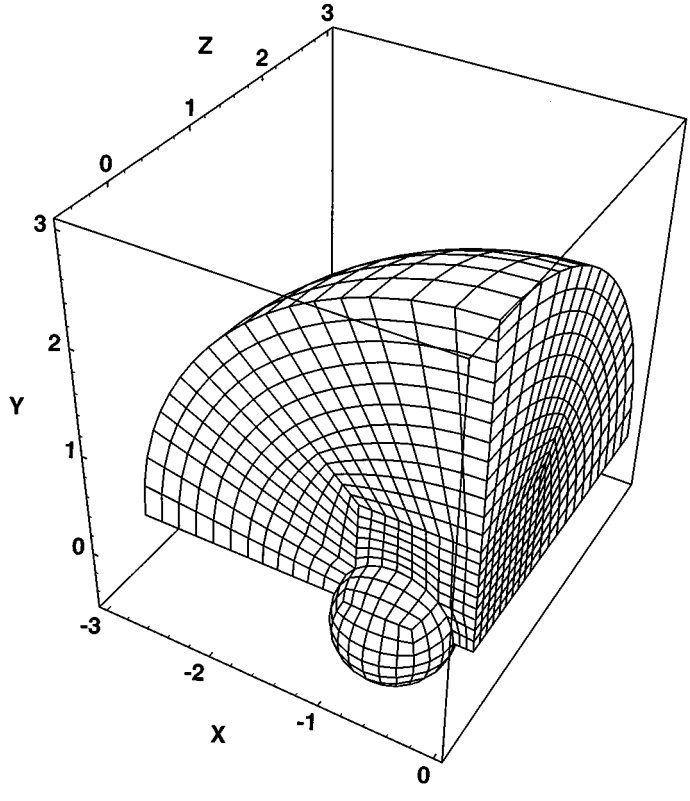

FIG. 1. Sample hexahedral grid of a dielectric sphere embedded in a spherical volume.

TABLE I
Conductivity Values for Maxwellian Absorber

Layer	1	2	3	4	5	6
σ	1.25	5.0	11.25	20.0	31.25	45.0

with a smooth $\cos^2$ cross section. The time dependence of the source is given by

$$E(t) = \left(1 - \exp\left(-\frac{t}{2\tau}\right)^2\right) \sin(\omega t). \tag{58}$$

The parameter τ determines the rise time of the beam, typically τ is chosen to be four periods. The simulation is typically run for twelve periods at a sampling rate of 50 samples per period. This is enough time for the simulation to reach steady state.

The computational grid is terminated with a Maxwellian absorber in order to simulate an infinite medium [32, 33]. In this paper a Maxwellian absorber is defined as several layers of artificial anisotropic media, with the conductivity of the layers graded in such a way as to reduce reflections from the boundary. This can be interpreted as an impedance matching device. In a Maxwellian absorber the electric conductivity σ_E and the magnetic conductivity σ_M are equal. In this paper a uniaxial tensor conductivity is employed with the optical axis normal to the boundary of the computational grid. The conductivity in along the optical axis is zero, the conductivity normal to this axis is given in Table I. The permittivity and permeability are those of free space. The choice of a spherical outer boundary simplifies the implementation of the Maxwellian absorber and results in excellent absorbtion of the nearly spherical scattered fields. Note that a spherical outer boundary is not required, and that the method used here does not require an orthogonal or structured grid.

The Maxwellian absorber used in this paper is quite different from the perfectly matched layer (PML) schemes used in the FDTD community. Although these PML schemes also use multiple layers with varying conductivity, they result in a modifed split-field PDE which has been shown to be weakly unstable. Some frequency domain PML schemes use active media in an attempt to achieve perfect absorbtion, but these schemes also result in instabilities when applied to temporal electromagnetics. The Maxwellian absorber used here does not modify the variational form of Maxwell's equations, nor does it employ active media in an attempt to achieve perfect matching. When used in a semi-implicit leapfrog update as in (34) and (35) the Maxwellian absorber is a simple and stable approach for reducing the scattering from the truncation of the computational grid. The time-dependent source used to launch the wave into the domain is applied to the grid surface seperating the absorber from the interior of the domain; this is the outer surface shown in Fig. 1.

Given the electromagnetic fields in the vicinity of the dielectric object the net force on the object is calculated using the Maxwell stress tensor. The Maxwell stress tensor $\bar{T}$ is given by

$$\bar{T} = \frac{1}{2}(\vec{D} \cdot \vec{E} + \vec{B} \cdot \vec{H})\bar{I} - (\vec{D}\vec{E} + \vec{B}\vec{H}), \tag{59}$$

where $\bar{I}$ is the identity tensor. The net force on the dielectric object is then

$$\vec{F} = \oint_{\Gamma} \bar{T} \cdot \hat{n}\, d\Gamma, \tag{60}$$

where Γ is the surface surrounding the object and $\hat{n}$ is the unit surface normal. The integral is computed using a two-dimensional trapezoidal rule. The Maxwell stress tensor is not continuous across the dielectric discontinuity; in (60) the fields are evaluated on the vaccuum side of the interface. The basis for this approach is that it gives the correct answer for the extreme case of scattering by a perfect conductor, which would have zero fields on the inside surface.

In order for there to be a significant net force, there must be a significant gradient in the electromagnetic field, hence the terminology optical gradient trap. In electrostatics it is known that a dielectric body will tend to move toward regions of increasing electric field, since this reduces the total electrostatic energy of the system. The electrostatic force is proportional to $\nabla(\vec{E} \cdot \vec{E})$. An optical gradient trap operates analogously, with the exception that it is an electromagnetic phenomenon rather than an electrostatic one. It is important to note that the force computed via (60) is time varying, but the inertia of the dielectric object is such that it cannot possibly respond to the rapidly fluctuating fields. Thus the optical force that is measured in the laboratory is a time-averaged force. The calculation of the stress and the net force is straightforward; any error in the force calculation is due to error in the electromagnetic fields, which is determined by the grid spacing and the performance of the Maxwellian absorber. Based on previous computational experiments in which computed electromagnetic fields are compared to analytical results it is estimated that the electromagnetic fields are correct to within 10% [26] for a grid density of six cells per wavelength.

4.1. *Axial Trapping of Microspheres*

A dielectric object can be trapped below the focus spot on the axis of the laser beam. This is referred to as axial trapping. The geometry of axial trapping is illustrated in Fig. 2. The electromagnetic energy gradient is toward the focus spot, so there is a possibility that the dielectric object will be pulled toward the focus. A strong electromagnetic energy gradient is a necessary, but not sufficient, condition for trapping to occur. The incident laser beam is both reflected and refracted by the dielectric object, resulting in a back-scattered field and a forward scattered field. The net force on the dielectric object will be toward the focus spot only if there is a significant amount of forward scattering. The amount of forward scattering depends on the size and dielectric constant of the object, the cone angle of the laser beam,

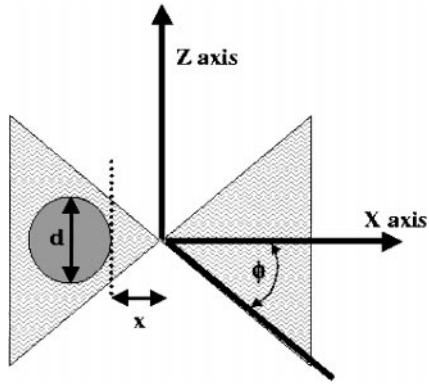

FIG. 2. Geometry of axial trapping experiments.

and the position of the object with respect to the focus spot. For axial trapping the force is independent of the polarization of the laser.

In the following computational experiments $\lambda = 1.0\,\mu$m, $d = 1.0\,\mu$m, $x = 0.4\,\mu$m, and $\theta = 45^\circ$. The laser rise time τ was equal to four periods and the fields were sampled 50 times per period, which is well below the time step required for stability. The small time step is employed for an accurate computation of the time-averaged force on the object. The fields were updated for twelve periods, or 600 time steps. The simulation was performed using a variety of dielectric constants in order to determine the effect of dielectric constant on the optical trapping efficiency. As a reference illustration, Fig. 11 shows a snapshot of the electric field intensity for the case of $\epsilon = 1.0$; the dielectric object is invisible for all intents and purposes. The incident laser beam is propagating in the negative x direction, with the focus spot at the center of the computation mesh. Figure 12 shows the electric field intensity for a dielectric constant of $\epsilon = 1.2$. In Fig. 12 the forward scattered field is amplified compared to the incident field; hence the momentum in the axial direction is qualitatively greater than the momentum in the incident beam and there is a net force on the object toward the focus spot. Since the enhanced forward scattering in Fig. 12 is subtle, the difference between Figs. 12 and 11 is shown in Fig. 13 with a change in scale.

The scattered field is amplified for only a small range of dielectric constants. Snapshots of the electric field intensity for dielectric constants of $\epsilon = 2.0$ and $\epsilon = 5.0$ are shown in Figs. 14 and 15. In Fig. 14 the forward-scattered field is slightly diminished, and qualitatively the object will be pushed away from the focus. In Fig. 15 the forward-scattered field is significantly diminished, the laser beam is essentially reflected by the dielectric sphere, and conservation of momentum implies that the sphere will again be pushed away from the focus spot in the negative x direction.

The time-averaged net force on the dielectric sphere was computed via (60) for dielectric constants ranging from 1.0 to 2.0. The optical trapping efficiency Q is shown versus dielectric constant in Fig. 3. The dielectric sphere is trapped (positive Q) for epsilon ranging from

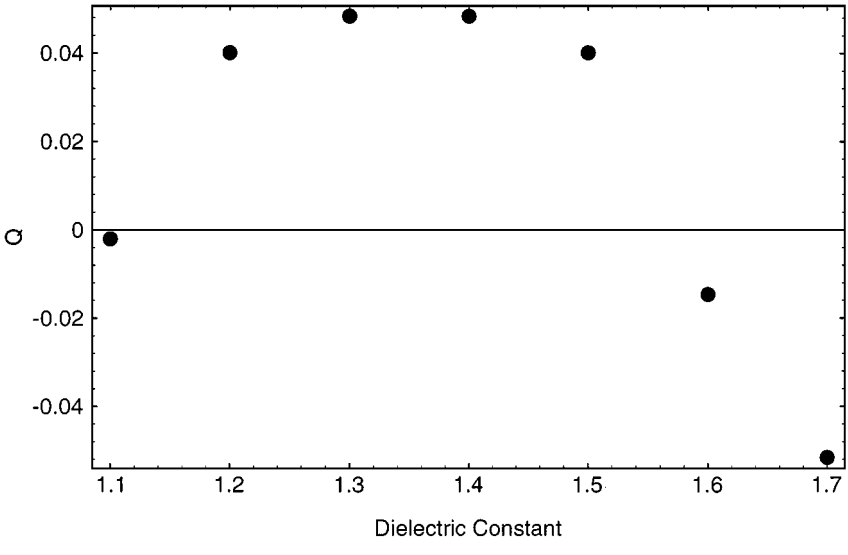

FIG. 3. Computed axial trapping efficiency Q vs relative dielectric constant. Parameters $\lambda = 1.0\,\mu$m, $d = 1.0\,\mu$m, $x = 0.4\,\mu$m, and $\theta = 45^\circ$.

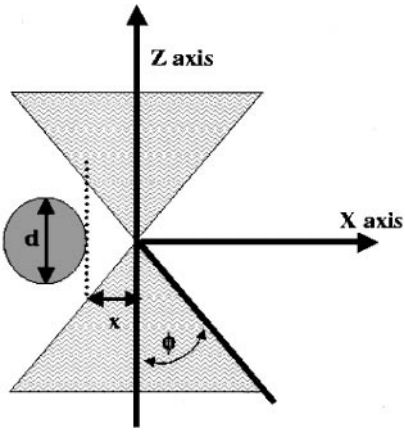

FIG. 4. Geometry of transverse trapping experiments.

1.12 to 1.55. For $\epsilon < 1.1$ the dielectric sphere does not refract the fields enough to have a significant effect on the propagation of the beam, for $\epsilon > 1.55$ there is significant back scattering of the beam and the dielectric sphere is pushed away from the focus. The computed Q values presented here are comparable to the measured results presented in [4]. Note that in [4] the axial force was measured in water; hence the dielectric constant used in this paper should be considered relative to the background dielectric. The amorphous silica spheres used in [4] had a relative dielectric constant of 1.12. For this value of ϵ we compute a Q of 0.008, compared to a measured Q of $0.006 +/- 0.001$. Also note that in [4] the dielectric sphere is free to move and hence the focus spot x is not fixed in the experimental setup.

4.2. *Transverse Trapping of Microspheres*

A dielectric object can also be trapped transversely, with the object adjacent, the focus spot rather than below it. The geometry of transverse trapping is illustrated in Fig. 4.

Again, the electromagnetic energy gradient is toward the focus spot, so there is a possibility that the dielectric object will be pulled toward the focus. The parameters for this experiment are identical to those for the axial trapping experiment above, except for the orientation of the laser beam. In addition, this computational experiment is performed for two different polarizations of the incident laser beam since the geometry is not symmetric. As a reference illustration, Fig. 16 shows a snapshot of the electric field intensity for a dielectric constant of $\epsilon = 1.0$; the dielectric sphere is for all intents and purposes invisible to the laser beam. The laser beam is propagating in the negative z direction, with the focus spot again at the center of the computational mesh. The electric field is polarized in the x direction. Figures 17 and 18 show the electric field intensity for dielectric constants of $\epsilon = 1.2$ and $\epsilon = 2.0$, respectively. These figures are snapshots of the field at the same instant of time. Note that the laser beam is refracted toward the left (negative x direction), opposite of what occurs in an off-center billiard ball collision. Hence, qualitatively, conservation of momentum implies that the dielectric microsphere is pulled toward the focus spot. Figure 19 shows the electric field intensity for a dielectric constant of $\epsilon = 5.0$. In this figure the laser beam is clearly reflected toward the right (positive x direction), and conservation of momentum implies that the dielectric sphere will be pushed away from the focus spot.

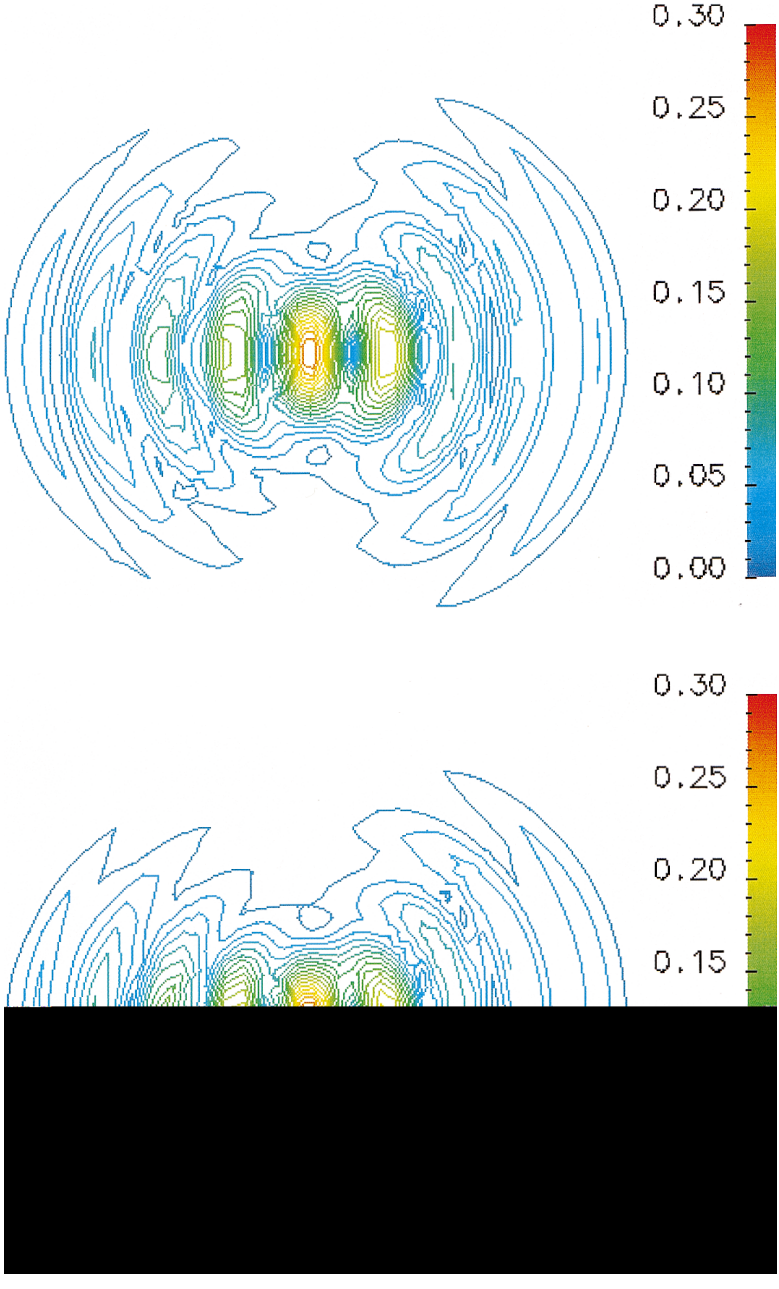

FIG. 11. Snapshot of electric field intensity for $\epsilon = 1.0$ microsphere, axial experiment.

FIG. 12. Snapshot of electric field intensity for $\epsilon = 1.2$ microsphere, axial experiment.

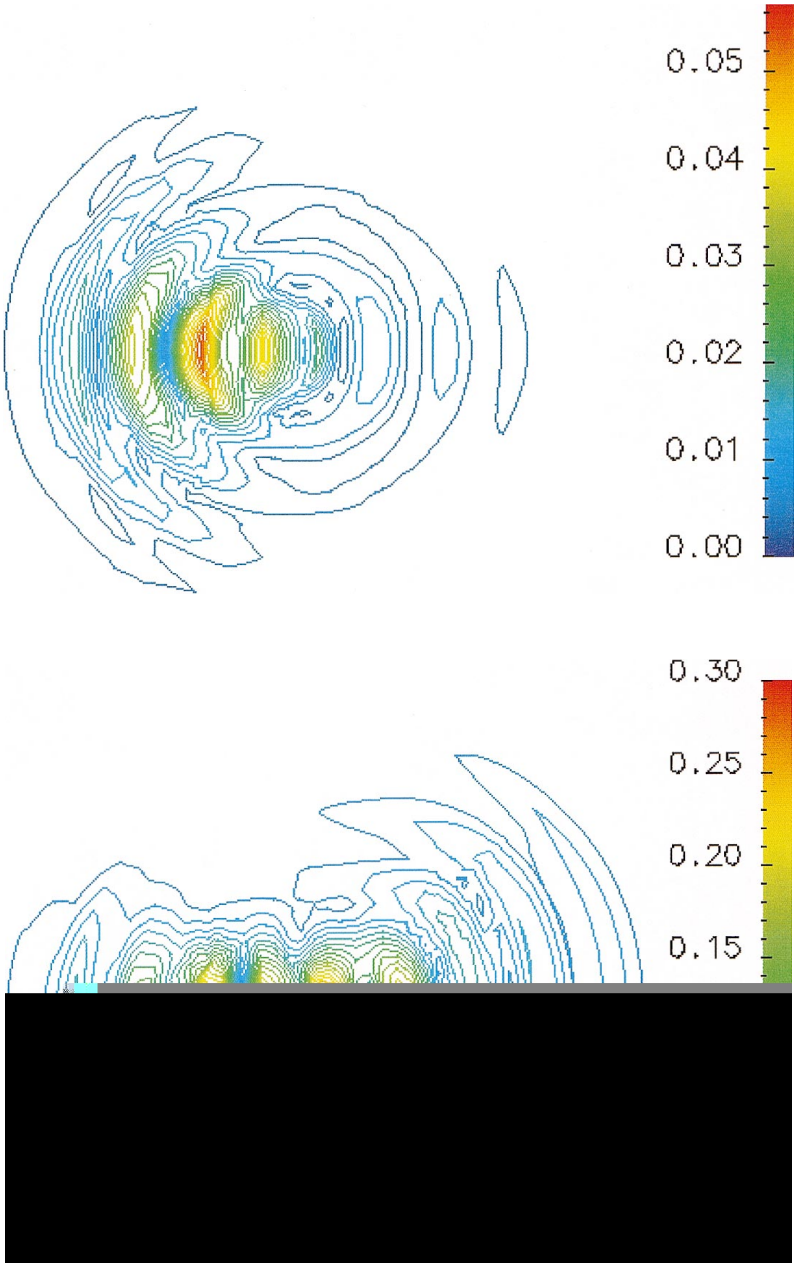

FIG. 13. Difference between the $\epsilon = 1.2$ and $\epsilon = 1.0$ electric fields clearly shows enhanced forward scattering.

FIG. 14. Snapshot of electric field intensity for $\epsilon = 2.0$ microsphere, axial experiment.

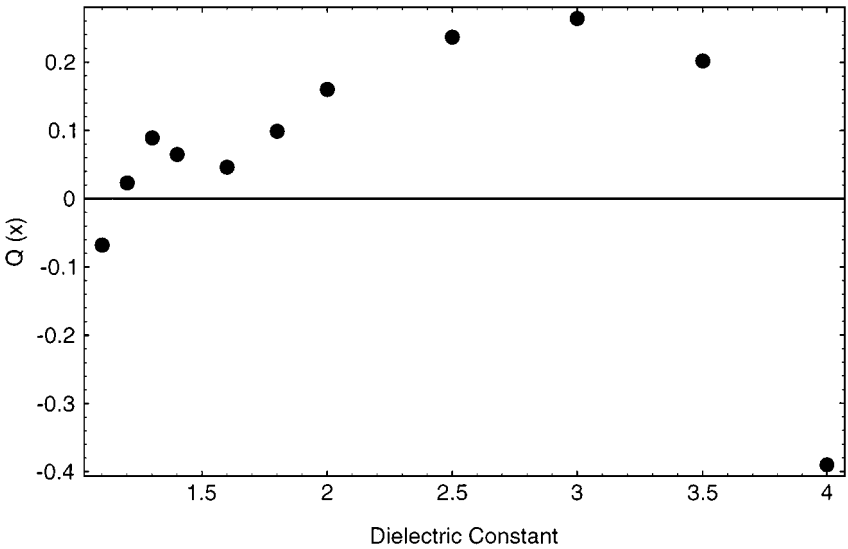

FIG. 5. Computed transverse trapping efficiency Q_x vs relative dielectric constant, x polarization. Parameters $\lambda = 1.0\,\mu$m, $d = 1.0\,\mu$m, $x = 0.4\,\mu$m, and $\theta = 45^\circ$.

The time-averaged net force on the dielectric sphere is computed in exactly the same manner for the transverse experiment as for the axial experiment. The force was computed via (60) for dielectric constants ranging from 1.0 to 4.0. For the transverse trapping experiments the computed force has both x and z components, and it is difficult to define a single trapping efficiency Q. Instead, we define

$$Q_x = \frac{cF_x}{nP}, \qquad Q_z = \frac{cF_z}{nP}, \tag{61}$$

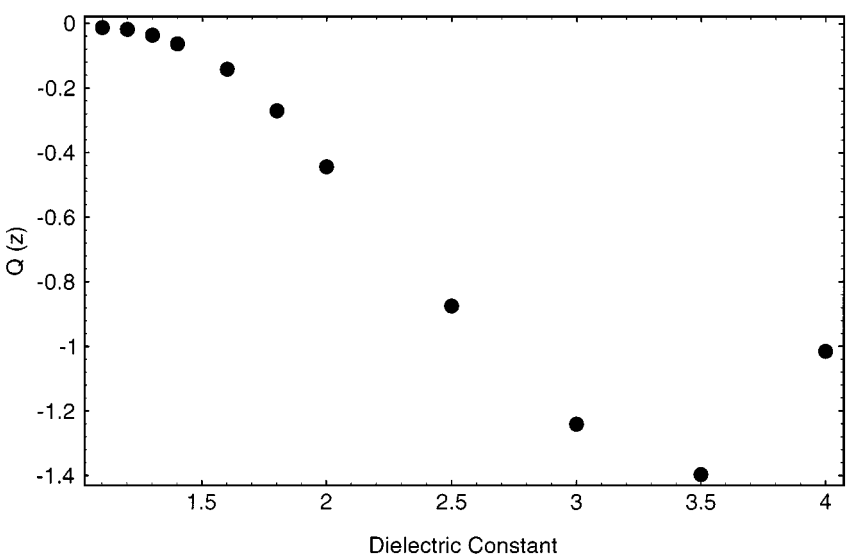

FIG. 6. Computed transverse trapping efficiency Q_z vs relative dielectric constant, x polarization. Parameters $\lambda = 0\,\mu$m, $d = 1.0\,\mu$m, $x = 0.4\,\mu$m, and $\theta = 45^\circ$.

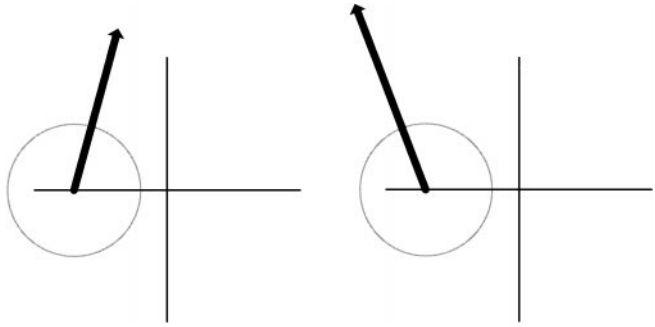

FIG. 7. Computed vector force on the dielectric sphere for the transverse trapping experiment, x polarization. The left figure is for $\epsilon = 3.0$; the right is for $\epsilon = 4.0$.

where F_x and F_z are the x and z components of the force, respectively. These Q's are shown in Figs. 5 and 6. A positive Q_x means that the x component of the force is toward the focus spot, and Fig. 5 illustrates that the dielectric sphere will be pulled toward the focus for particular values of the dielectric constant. Comparing to the axial trapping experiment, we note that the magnitude of the optical forces for the transverse experiment are significantly greater than that obtained for the axial experiment. This is in qualitative agreement with the measured results in [4], which report transverse trapping efficiencies of 0.15, compared to 0.006 for the axial experiment. In addition, the sphere is pulled toward the focus for a large range of dielectric constant, approximately $1.1 < \epsilon < 3.7$. This phenomenon has not yet been verified experimentally. It is not clear exactly for what range of dielectric constant the particle is actually trapped by the laser beam. For example, at $\epsilon = 3.0$, $Q_x > 0$ and the sphere is pulled toward the axis of the laser beam, but $Q_z < 0$ and the sphere is pushed away from the focus spot. On the other hand, at $\epsilon = 4.0$ both $Q_x < 0$ and $Q_z < 0$, and the sphere is clearly not trapped. These forces are illustrated graphically in Fig. 7 for $\epsilon = 3.0$ and $\epsilon = 4.0$. The optical scattering changes character at approximately $\epsilon = 3.7$.

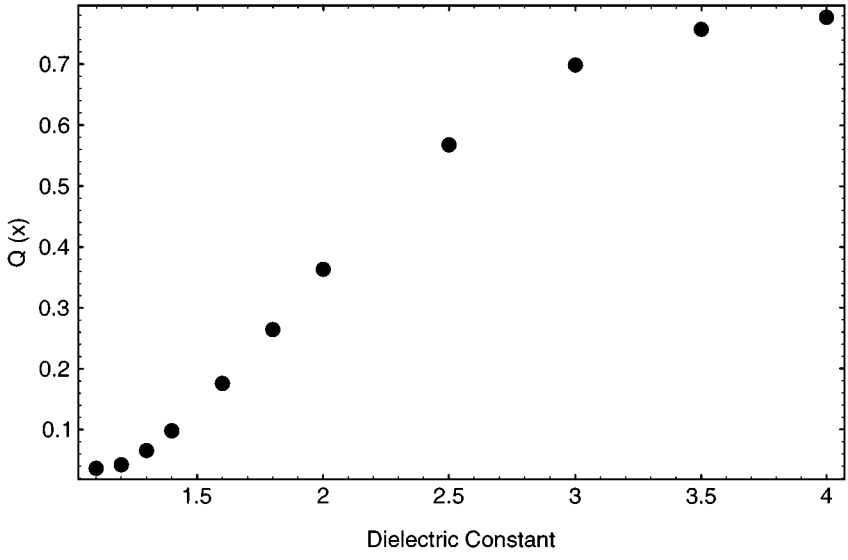

FIG. 8. Computed transverse trapping efficiency Q_x vs relative dielectric constant, y polarization. Parameters $\lambda = 1.0\,\mu$m, $d = 1.0\,\mu$m, $x = 0.4\,\mu$m, and $\theta = 45^\circ$.

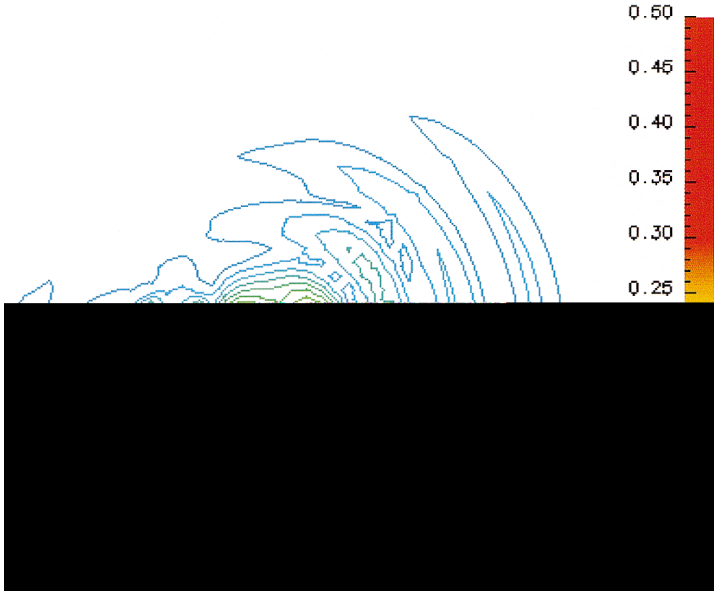

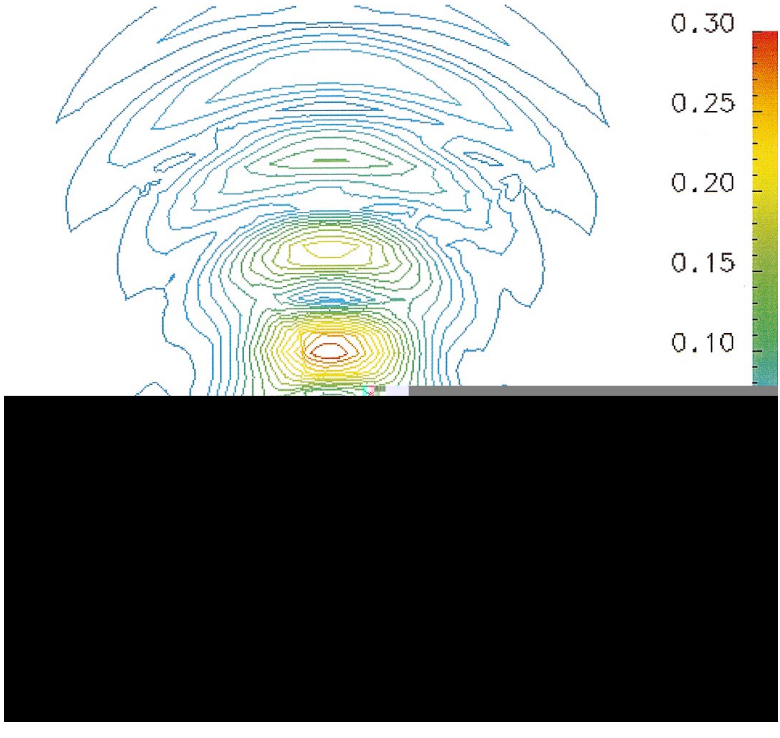

FIG. 15. Snapshot of electric field intensity for $\epsilon = 5.0$ microsphere, axial experiment.

FIG. 16. Snapshot of electric field intensity for $\epsilon = 1.0$ microsphere, transverse experiment, x polarization.

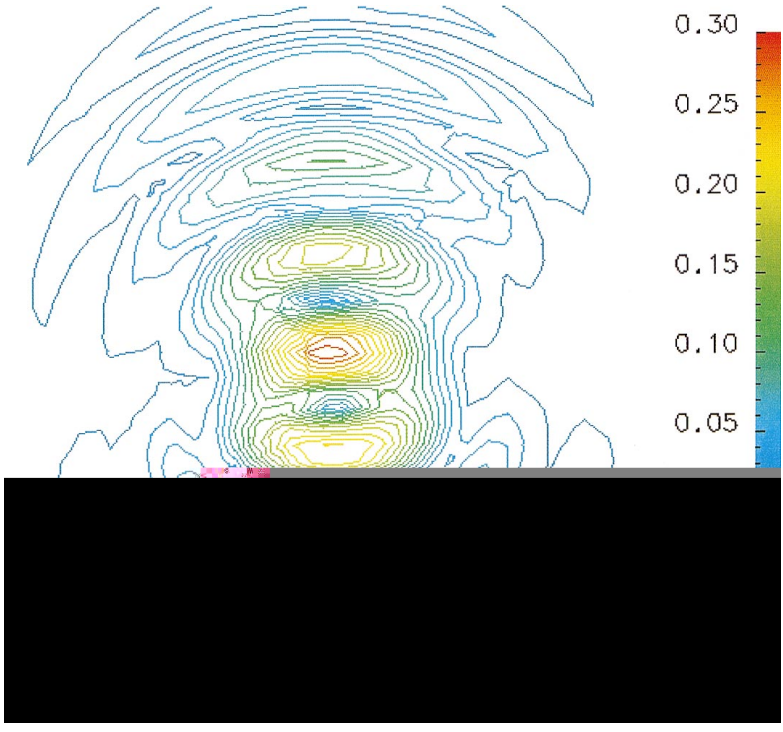

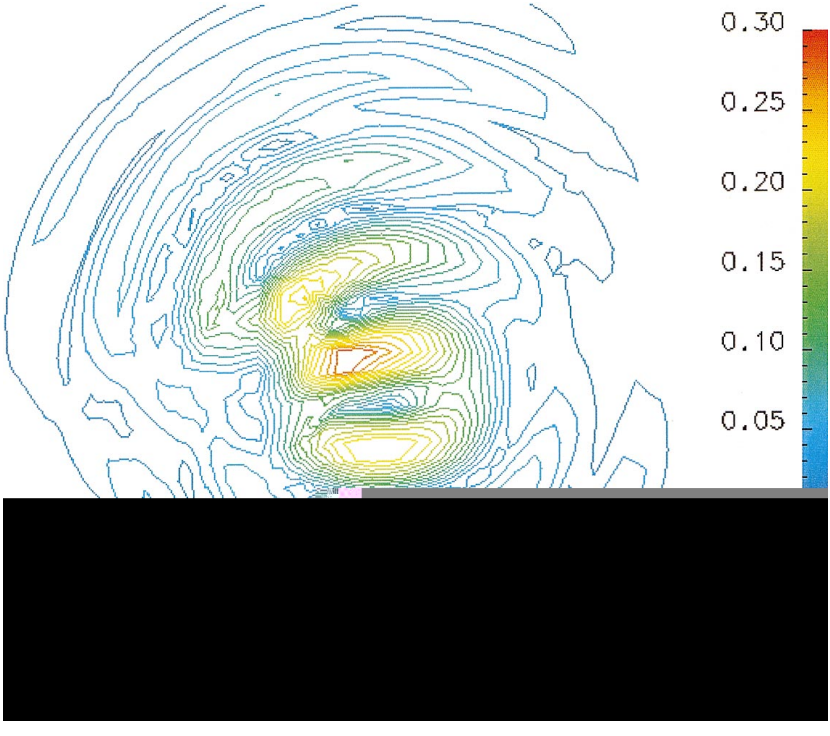

FIG. 17. Snapshot of electric field intensity for $\epsilon = 1.2$ microsphere, transverse experiment, x polarization.

FIG. 18. Snapshot of electric field intensity for $\epsilon = 2.0$ microsphere, transverse experiment, x polarization.

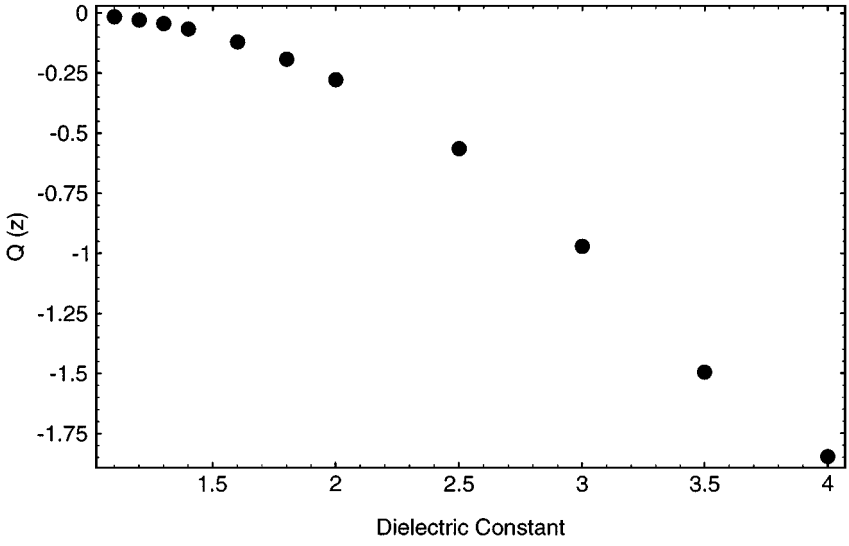

FIG. 9. Computed transverse trapping efficiency Q_z vs relative dielectric constant, *y* polarization. Parameters $\lambda = 1.0\,\mu$m, $d = 1.0\,\mu$m, $x = 0.4\,\mu$m, and $\theta = 45^\circ$.

The above transverse trapping experiment was repeated for the case of electric field polarized in the *y* direction. Snapshots of the electric field intensity are shown in Figs. 20, 21, and 22 corresponding to dielectric constants of 1.2, 2.0, and 10.0, respectively. For $\epsilon = 1.2$ and $\epsilon = 2.0$ the scattered field is quite similar to that obtained for the *x* polarization experiment; again the laser beam is refracted toward the left (negative *x* direction), opposite of what occurs in an off-center billiard ball collison. However, the scattering did not change character as the dielectric constant increased as it did for the *x* polarization experiment. The laser beam was refracted more and more as ϵ increased. This difference between the *x* and *y* polarization experiments is analogous to plane–plane wave refraction at a dielectric interface, where one polarization exhibits a change of character at a critical value of dielectric constant (brewster angle for transverse electric polarization) and the other polarization does not.

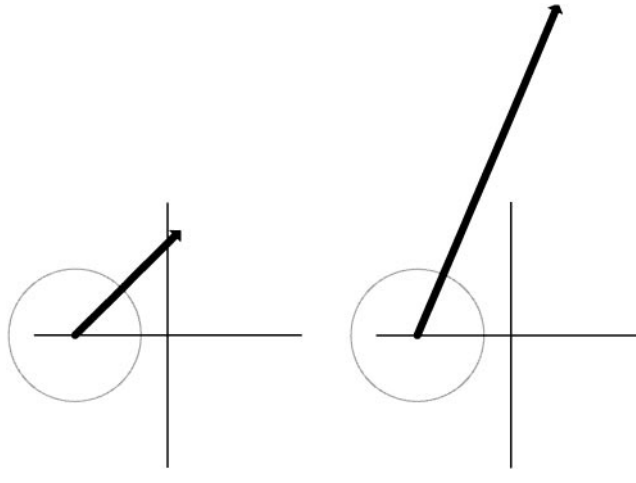

FIG. 10. Computed vector force on the dielectric sphere for the transverse trapping experiment, *x* polarization. The left figure is for $\epsilon = 3.0$; the right is for $\epsilon = 4.0$.

The time-averaged net force on the dielectric sphere is again computed for a range of dielectric constants from 1.0 to 4.0. The x- and z-directed forces are converted to Q's via (61), and these Q's are shown in Figs. 8 and 9. The z component of Q is quite similar to that obtained for the x polarization experiment; it is negative for all values of dielectric constant. The x component of Q differs from that obtained for the x polarization experiment in that it remains positive for all values of dielectric constant. This means that the sphere is always pulled toward the axis of the beam. Again, it is not clear exactly for what range of dielectric constant the sphere is actually trapped by the beam. The vector optical force is illustrated graphically in Fig. 10 for $\epsilon = 3.0$ and $\epsilon = 4.0$ and shows that the optical scattering does not have an abrupt change of character. However, the z component of the force becomes dominant and it will ultimately be pushed away from the focus spot as the dielectric constant increases.

5. SUMMARY

An unstructured-grid vector finite element is used for the numerical modeling of optical gradient traps. The method uses edge vector finite elements as a basis for the electric field and face vector finite elements as a basis for the magnetic flux density. This choice of basis functions allows for the proper modeling of continuity (discontinuity) of the tangential (normal) components of the electric field across material discontinuities. In addition, this choice of basis functions prevents spurious irrotational fields from polluting the solution. The method allows for tensor permeability, permittivity, and electric and magnetic conductivities. Thus it is a simple matter to implement a Maxwellian absorber to attenuate outgoing electromagnetic waves. A second-order central-difference method is used to advance the fields and fluxes in a leapfrog manner. The method is shown to be stable and energy conserving, assuming the time step is chosen according to a Nyquist condition.

A 3D unstructured hexahedral grid is used to model the dielectric object and the surrounding space. A laser beam is launched into the computational grid by a time varying source. As the electromagnetic fields are evolved, the net force on the dielectric object is computed by integrating the Maxwell stress tensor over the surface of the object. The net force is a function of time, but since the dielectric object cannot possibly respond to optical frequencies the time-averaged force is computed. The computed optical trapping efficiencies are computed for both axial and transverse trapping geometries for a 1-μm sphere, using a range of dielectric constants. A simple sphere is used so that the computed results can be compared to previously measured data. The comparison is quite favorable considering the differences between the computational experiment (object location is fixed with respect to the beam) and the physical experiment (object is free to move in response to the beam).

Optical trapping efficiencies of up to $Q = 0.05$ were obtained for a relative dielectric constant of $\epsilon = 1.4$ for the axial trapping experiment. We show that the object is trapped only when $1.1 < \epsilon < 1.55$. By examining the electric fields it is clear that the forward scattering is enhanced for this range of dielectric constant. For $\epsilon < 1.1$ it appears that the sphere is not refractive enough to scatter the beam, whereas for $\epsilon > 1.55$ the beam is essentially reflected from the object, pushing the object away from the focus. The amorphous silica spheres used in the measurements [4] had a relative dielectric constant of 1.12. For this value of ϵ, we compute a Q of 0.008, compared to a measured Q of $0.006 +/- 0.001$.

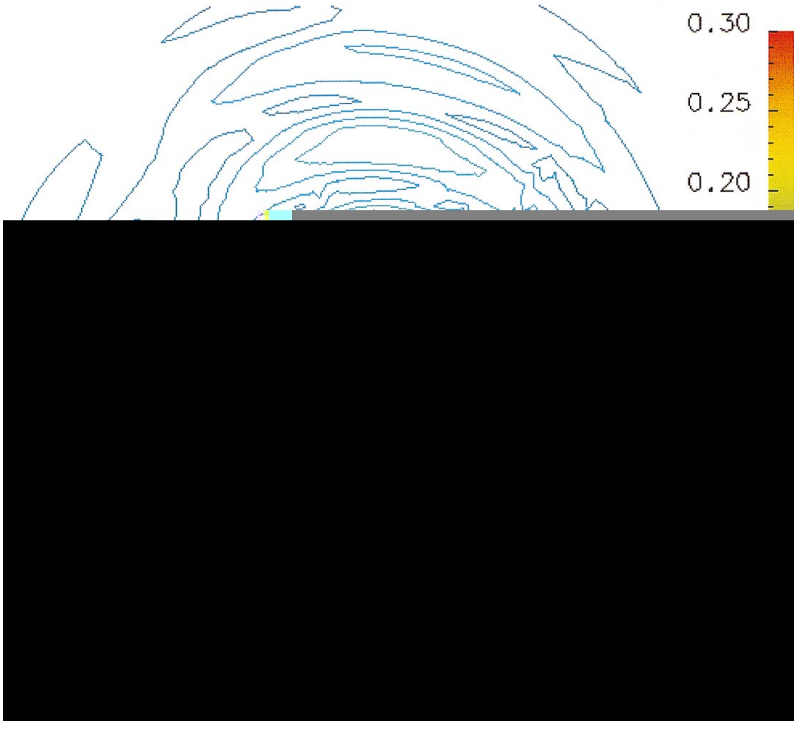

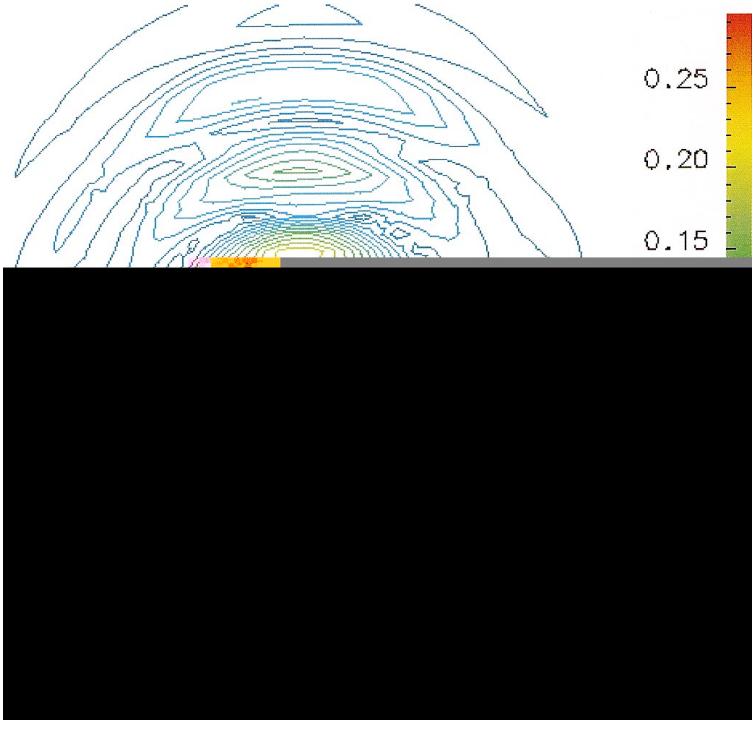

FIG. 19. Snapshot of electric field intensity for $\epsilon = 5.0$ microsphere, transverse experiment, x polarization.

FIG. 20. Snapshot of electric field intensity for $\epsilon = 1.2$ microsphere, transverse experiment, y polarization.

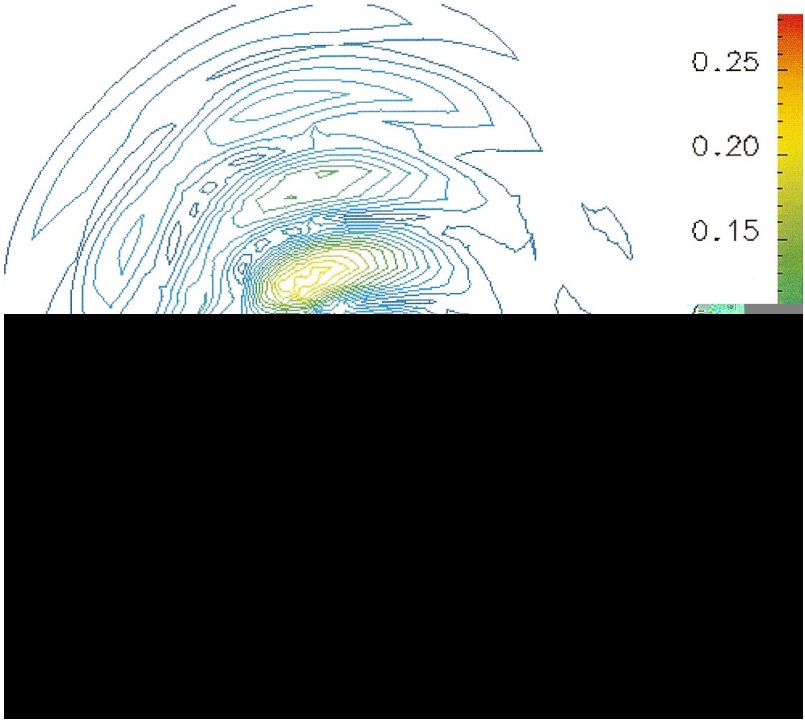

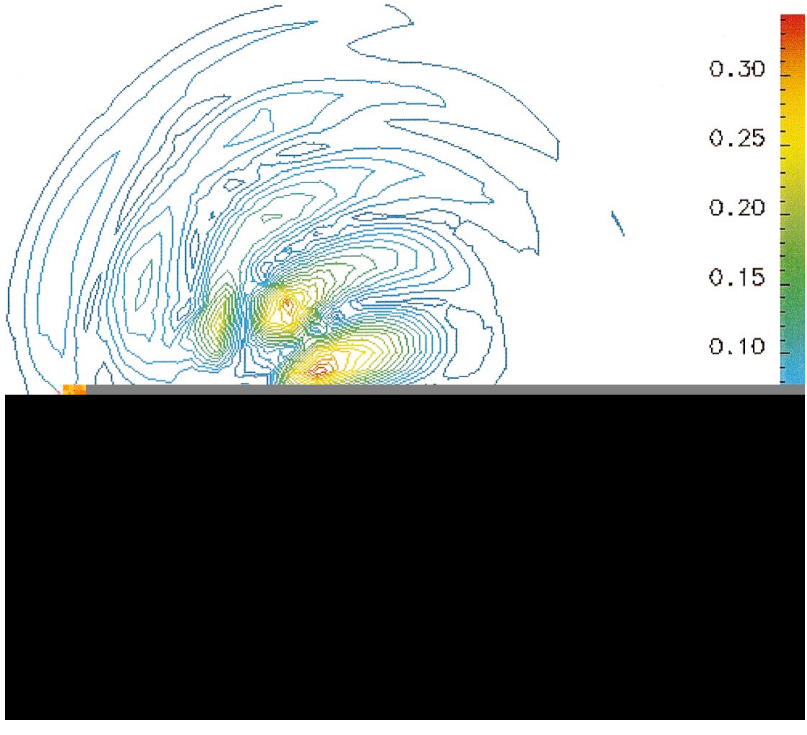

FIG. 21. Snapshot of electric field intensity for $\epsilon = 2.0$ microsphere, transverse experiment, y polarization.

FIG. 22. Snapshot of electric field intensity for $\epsilon = 5.0$ microsphere, transverse experiment, y polarization.

The simulations of the transverse trapping experiments were quite interesting. We show that the scattered field is refracted such that the electromagnetic momentum behaves opposite of what occurs in an off-center billiard ball collision. With simple conservation of momentum arguments, this explains how the dielectric object is pulled toward the focus spot. However, this effect was polarization dependent. For the x polarization the laser beam is refracted only for particular values of dielectric constant. When the dielectric constant was increased beyond a critical value of $\epsilon = 3.7$ the beam was reflected from the object. This phenomenon was qualitatively visible in the field intensity plots and quantitatively visible as a change in sign of the net optical force on the object. The y-polarized laser beam, on the other hand, was refracted more and more as the dielectric constant was increased. For both polarizations, the optical trapping force was significantly greater that the transverse trapping force, which is in agreement with the measured results in [4]. However, for the transverse trapping experiments we had difficulty defining a single optical trapping efficiency Q, since the optical force had components in both the x and z directions. If $Q_x < 0$ it is clear that the object is pushed away from the focus spot. It is not clear what happens when $Q_x > 0$ and $Q_z < 0$. To resolve this issue it is necessary to have the sphere actually move in response to the laser beam, but this represents a significant effort and was beyond the goals of this project.

REFERENCES

1. A. Ashkin, Acceleration and trapping of particles by radiation pressure, *Phys. Rev. Lett.* **24**, 156 (1970).
2. A. Ashkin and J. M. Dziedzic, Optical levitation by radiation pressure, *Appl. Phys. Lett.* **19**, 283 (1971).
3. A. Ashkin, J. M. Dziedzic, E. J. Bjorkholm, and S. Chu, Observation of a single-beam gradient optical trap for dielectric particles, *Opt. Lett.* **11**, 288 (1986).
4. W. H. Wright, G. J. Sonek, and M. W. Berns, Parametric study of the force on microspheres help by optical tweezers, *Appl. Opt.* **33**, 1753 (1994).
5. C. D'Helon, E. W. Dearden, H. Rubenstein-Dunlop, and N. R. Heckenberg, Measurement of the optical force and trapping range of a single-beam gradient optical trap for micron-sized latex spheres, *J. Mod. Opt.* **41**, 595 (1994).
6. R. Omori, T. Kobayashi, and A. Suzuki, Observation of a single-beam gradient force optical trap for dielectric particles in air, *Opt. Lett.* **22**, 816 (1997).
7. T. N. Buican, M. J. Smith, H. A. Crissman, G. C. Salzman, C. C. stewart, and J. C. Martin, Automated single-cell manipulation and sorting by light trapping, *Appl. Opt.* **26**, 5311 (1987).
8. A. Ashkin, J. M. Dziedzic, and T. M. Yamane, Optical trapping and manipulation of single cells using infrared laser beams, *Nature* **330**, 769 (1987).
9. Y. Tadir, W. H. Wright, O. Vafa, T. Ord, R. H. Asch, and M. W. Berns, Micromanipulation of sperm by a laser generated optical trap, *Fert. Ster.* **57**, 870 (1989).
10. A. Ashkin and J. M. Dziedzic, Optical trapping and manipulation of viruses abd bacteria, *Science* **235**, 1517 (1987).
11. S. M. Block, D. F. Blair, and H. C. Berg, Compliance of bacterial polyhooks measured with optical tweezers, *Cytometry* **12**, 492 (1991).
12. A. Ashkin, K. Schultze, J. M. Dziedzic, U. Euteneur, and M. Schliwa, Force generation of organelle transport measured *in vivo* by an infrared laser trap, *Nature* **348**, 346 (1990).
13. S. C. Kuo and M. P. Sheetz, Force of single kinesin molecules measured with optical tweezers, *Science* **260**, 232 (1993).
14. S. Block, L. S. B. Goldstein, and B. J. Schnapp, Using optical tweezers to investigate kinesin-based motility *in vitro*, *J. Cell Bio.* **109**, 81a (1989).

15. A. Ashkin, Forces of a single-beam gradient laser trap on a dielectric sphere in the ray optics regime, *Bio. J.* **61**, 569 (1992).
16. R. C. Gauthier and S. Wallace, Optical levitation of spheres: analytical development and numerical computations of the force equations, *J. Opt. Soc. Am. B* **12** (1995).
17. R. C. Gauthier, Theoretical investigation of the optical trapping force and torque on cylindrical micro-objects, *J. Opt. Soc. Am. B* **14** (1997).
18. J. P. Barton, D. R. Alexander, and S. A. Schaub, Internal and near-surface electromagnetic fields for a spherical particle irradiated by a focused laser beam, *J. Appl. Phys.* **64**, 1632 (1988).
19. J. P. Barton, D. R. Alexander, and S. A. Schaub, Theoretical determination of net radiation force and torge for a spherical particle illuminated by a focused laser beam, *J. Appl. Phys.* **66**, 4594 (1989).
20. J. P. Barton and D. R. Alexander, Fifth-order corrected electromagnetic field components for a fundamental Gaussian beam, *J. Appl. Phys.* **66**, 2800 (1989).
21. Nedelec, J. C., Mixed finite elements in R3, *Numer. Math.* **35**, 315 (1980).
22. P. Monk, A. comparison of three mixed methods for the time-dependent Maxwell's equations, *SIAM J. Sci. Stat. Comput.* **13**, 1097 (1992).
23. P. Monk, An analysis of Nedelec's method for the spatial discretization of Maxwell's equations, *J. Comput. Appl. Math.* **47**, 101 (1993).
24. P. Monk and A. Parrot, A dispersion analysis of finite element methods for Maxwell's equations, *SIAM J. Sci. Comput.* **15**, 916 (1994).
25. G. Warren and W. Scott, An investigation of numerical dispersion in the vector finite element method using quadrilateral elements, *IEEE Trans. Ant. Prop.* **42**, 1502 (1994).
26. D. White, *Discrete Time Vector Finite Element Methods for Solving Maxwell's Equations on 3D Unstructured Grids*, Ph.D. dissertation, University of California at Davis, 1997.
27. Z. Cendes, Vector finite elements for electromagnetic field calculations, *IEEE Trans. Mag.* **27**, 3958 (1991).
28. D. Sun, J. Magnes, X. Yuan, and Z. Cendes, Spurious modes in finite element methods, *IEEE Ant. Prop. Mag.* **37**, 12 (1995).
29. D. A. White, Solution of capacitance systems using incomplete Cholesky fixed point iteration, submitted for publication.
30. C. R. Evans and J. F. Hawley, Simulation of magnetohydrodynamic flows: A constrained transport method, *Astrophys. J.* **332**, 659 (1988).
31. N. K. Madsen, Divergence preserving discrete surface integral methods for Maxwell's equations using non-orthogonal unstructured grids, *J. Comput. Phys.* **119**, 34 (1995).
32. R. W. Ziolkowski, The design of maxwellian absorbers for numerical boundary conditions and for practical applications using engineered artificial materials, *IEEE Trans. Ant. Prop.* **45**, 656.
33. Z. Sachs, D. Kingsland, R. Lee, and J. Lee, A perfectly matched anisotropic absorber for use as an absorbing boundary condition, *IEEE Trans. Ant. Prop.* **43**, 1460.